Dynamic Force Reconstruction of Transient Flap Control Force Experiments in a Hypersonic Wind Tunnel

Jack W. Draper III*
Johns Hopkins University Applied Physics Laboratory, Laurel, MD, 20723, USA

Greg J. Brauckmann† and F. Drew Turbeville‡
NASA Langley Research Center, Hampton, VA, 23666, USA

Sung W. Lee§
University of Maryland, College Park, MD, 21040, USA

This work details the design of a sliced-cone model with a flap embedded within the slice. The flap is controlled by a fast acting servo to simulate a control force of a hypersonic vehicle. Design considerations such as sensor placement, expected loading, servo arm selection, and cavity temperatures are detailed in this work. Such a design imparts a dynamic response of the test article and as such, dynamic force measurement methodologies are required to reconstruct the control forcing. Three methods are of particular interest: the Sum of Weighted Accelerations Technique, Time Domain Deconvolution Method, and Frequency Domain Inverse Method. Novel versions of each method have been applied to this dataset to improve the reconstruction accuracy.

I. Nomenclature

$\hat{\mathbf{B}}$	=	impulse response matrix
C_A	=	dynamic calibration matrix
$C_{A,l}$	=	dynamic calibration matrix for resonant mode l
C_{Ax}	=	axial force coefficient of aerodynamic load
C_N	=	normal force coefficient of aerodynamic load
C_S	=	static calibration matrix
F_A	=	axial force of aerodynamic load
F_f	=	Force on the flap
F_N	=	normal force of aerodynamic load
F_{rec}	=	reconstructed force
H	=	frequency response function (FRF)
h	=	impulse response function (IRF)
M_∞	=	freestream Mach number
$\mathbf{N}_h$	=	shape matrix for IRF interpolation
$\hat{\mathbf{N}}_u$	=	shape matrix for input force interpolation
P_∞	=	freestream static pressure
P_{t1}	=	total pressure
P_{t2}	=	total pressure behind normal shock
q_∞	=	freestream dynamic pressure
R_1	=	IRF constraint parameter
R_2	=	input force constraint parameter
Re_∞	=	freestream Reynolds number

*Senior Engineer, Air and Missile Defense Sector, and Member AIAA.
†Aerospace Research Engineer, Aerothermodynamics Branch, Associate Fellow AIAA.
‡Aerospace Research Engineer, Aerothermodynamics Branch, Member AIAA.
§Professor, Department of Aerospace Engineering, and Associate Fellow AIAA.

Re_2 = Reynolds number behind normal shock
S_A = acceleration response data
$S_{A,l}$ = acceleration response data band pass filtered about resonant mode l
S_{ref} = reference area for force coefficients
S_S = strain response data
T_∞ = freestream temperature
T_{t1} = total temperature
t = time
Δt_s = sample time increment
U = Fourier transform of time domain dynamic input force u
U_∞ = freestream flow velocity
u = applied point force
$\mathbf{u}$ = dynamic input force matrix
Y = Fourier transform of time domain dynamic output response y
$\mathbf{y}$ = dynamic response matrix
y = time domain dynamic output response
α = test article angle of attack
ρ_∞ = Freestream flow density
ρ_2 = Flow density behind normal shock
τ_f = torque due to F_f
τ_s = servo torque
ω = frequency of interest

II. Introduction

This paper details the dynamic force reconstruction of a deployed flap into a hypersonic flow. A flap is embedded in a sliced cone model developed by the NASA Langley Research Center (LaRC), the Johns Hopkins University Applied Physics Laboratory (JHU/APL), and the University of Maryland (UMD). The deployment of this flap into a hypersonic flow is intended to simulate a control force of a hypersonic vehicle. The rapid deployment of the flap excites dynamics in the test article. Therefore, dynamic force measurement methodologies such as the Sum of Weighted Accelerations Technique (SWAT) [1–3], Time Domain Deconvolution Method (TDDM) [4, 5], and Frequency Domain Inverse Method (FDIM) [6–8] must be implemented.

Dynamic force measurement is applicable to a wide range of wind tunnel measurement scenarios such as supersonic combustion ramjet (scramjet) engine unstart [9–11], divert thruster firing [4–6], shroud separation [12, 13], and control surface deployment [14, 15]. Current measurement methodology typically assumes proportionality between strain and applied force [16]. When the force is approximately constant and the test article is steady, this is typically a good assumption. However, in the above examples and those detailed in this work, such an assumption is invalid. Due to the short duration or high frequency contribution of these example loads, a dynamic response is achieved. This response yields an elastic force contribution measurement rather than the applied aerodynamic force. The focus of this work is to demonstrate the SWAT, TDDM, and FDIM for a rapid control surface deflection example case in the NASA Langley Research Center 31-Inch Mach 10 wind tunnel [17]. The development of the dynamic force balance and demonstration of the measurement capability is intended to be a platform for future hypersonic dynamic force measurement experiments.

Many methods of dynamic signal reconstruction exist. However, due to the wide range of testing scenarios, limitations of each method, complexity of methodology formulation, and relative infancy of the interest in such measurement, no such "standard" method exists. Therefore, three dynamic force measurement techniques are of interest: the SWAT, TDDM, and FDIM. Marineau et al. [1, 2] successfully implemented a variant of the SWAT in the CUBRC facility on a small-scale hypersonic test article. The particular method of interest in this work is a further variant of the SWAT developed by Draper et al. [3] where modal separation and velocity scaling is assumed. The SWAT is a common technique as it builds on the static calibration techniques used for decades. However, it is somewhat unsuited for short duration and high frequency response facilities such as shock tunnels. For such facilities, the TDDM is more commonly used. Mee et al. [4, 5] used a variant of this method to measure the lift and drag of a test article in the T4 free-piston shock tunnel at the University of Queensland. In this work, a variant developed by Draper et al. [18, 19] is of interest. This method utilizes higher order deconvolution and least squares inversion to more easily solve the deconvolution

problem. The final method under investigation is the FDIM. This is a frequency domain couple to the TDDM and is less commonly used in hypersonic wind tunnel testing [20]. Grauer et al. [7] recently implemented a variant of this method to estimate control surface forcing for a T-2 airplane. The FDIM of interest in this work is a more simplified version detailed by Draper [21] that utilizes multiple calibration solution of the impulse response function (IRF).

Section III of this document overviews the experimental setup for these studies. A tunnel overview and a detailed overview of the design of the dynamic force balance is presented in this section. Additionally, the calibration procedure for the various force reconstruction methodologies is presented for additional clarity. The next section presents a brief overview of each of the three methods of interest for these studies. The following section presents real world considerations such as temperature, noise, distributed loading, and aeroelastic loading that can negatively affect measurements. The final section presents an overview of the wind tunnel results for each of the three methods. A comparison with expected values as well as with the typical strain gauge force measurement is presented to highlight the advantages of each method.

III. Experimental Setup

The calibration and wind-on tests are performed at the NASA LaRC 31-Inch Mach 10 wind tunnel. The test setup and results are presented for the studies in this tunnel. The primary investigation for these studies is reconstruction of the aerodynamic load applied during the deployment of a flap on the aft end of a sliced cone geometry. This could simulate a control force of a hypersonic vehicle. A load of this nature is highly dynamic and thus a dynamic force measurement methodology is required.

This section is subdivided into a variety of topics. First, an overview of the facility is presented to highlight the tunnel operation and capabilities of this particular test section. Next, an overview of the test article is presented. Upon review of this subsection, the operation of a given test and the inner workings of the test article are made clear. Following this, a more in depth overview of the hybrid dynamic force balance is presented. Finally, the dynamic calibration tests performed in this work are detailed.

A. Facility Overview

The experiments discussed in this subsection were performed at the NASA LaRC Mach 31-Inch 10 wind tunnel in March of 2023. A mock up of the tunnel is depicted in Figure 1 and was taken from Berger et al. [17]. The tunnel was built in 1957 and was originally designed for continuous operation. It was converted to a blow-down facility in the 1970s and continues to operate in that manner. The test section is a 31-inch square cross section. Run times of up to two minutes are capable in this tunnel with full use of the vacuum sphere. We make use of this long run time by pulsing the flap a number of times over the duration of the test. After parsing the data, this yields multiple data sets per wind tunnel run. Test articles are injected from the side of the test section after it has reached the desired conditions. The insertion time ranges from 1.25 to 4.2 seconds with acceleration magnitudes ranging from 0.3 to 3.3 gs depending on the injection speed. The slower speeds give more flexibility on model strength requirements as the injections loads will be smaller. Three rectangular optical ports are available to view the test section. One viewport is present in the injection plane. For these experiments, a high speed camera images the test section at a frame rate of 25 kFPS. These images are used to determine the angle achieved by the flap as it may differ from the commanded angle.

The nominal conditions for this tunnel can be seen in Table 1. Most tests are performed at condition 2 or 3 to simulate the Arnold Engineering Development Complex (AEDC) Wind Tunnel No. 9 (Tunnel 9) conditions while keeping the overall aerodynamic forcing magnitude within acceptable levels. All relevant information presented in this subsection was extracted from Berger et al. [17]. The reader may review this reference for more specifics on tunnel operation.

B. Test Article Overview

In this subsection, the overview of the test article under investigation for these experiments is presented. Additionally, some of the design considerations are discussed. The selected geometry for this study is a titanium 7° half-angle cone with a slice parallel to the flow on the aft end. The slice is located on the bottom of the cone. A picture of the mounted test article is shown in Figure 2. Embedded in the slice is a rectangular flap that can be deployed when commanded by the operators. Seven degree half-angle cones are very common throughout the history of wind tunnel testing and the flowfields are well understood for many conditions. Additionally, this cone-slice with ramp geometry is in line with future NASA LaRC testing objectives. Therefore, construction of this test article is useful not only for these studies, but

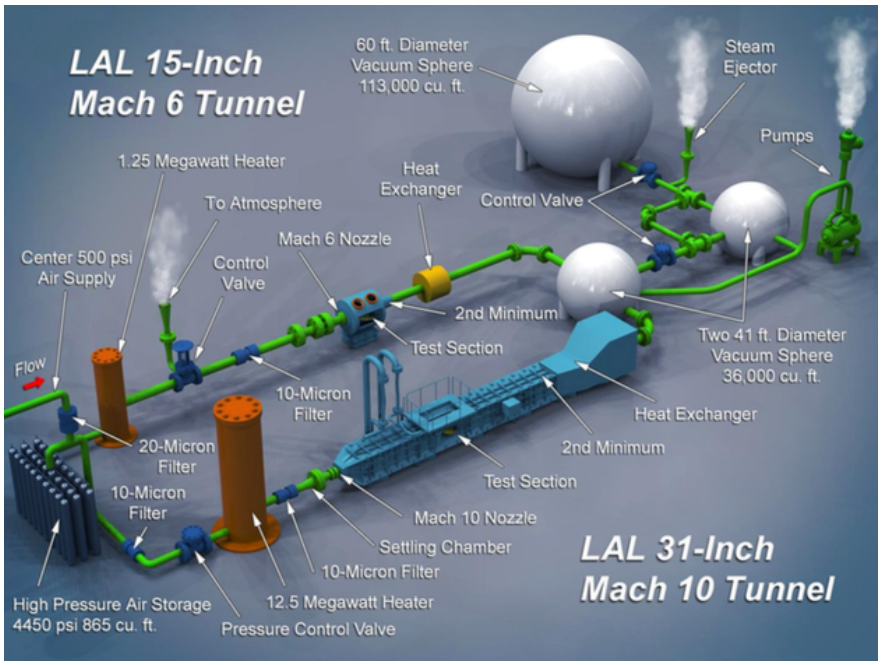


Fig. 1 NASA LaRC Mach 6 and 10 facility depiction [17].

Table 1 Nominal conditions for LaRC 31 inch Mach 10 air tunnel.

Variable	Unit	Condition 1	Condition 2	Condition 3	Condition 4
P_{t1}	(psi)	350	720	1300	1450
T_{t1}	($^\circ$R)	1775	1790	1790	1790
P_∞	(10^{-2} psi)	1	1.89	3.19	3.52
T_∞	($^\circ$R)	93.68	92.23	90.35	90.26
q_∞	(psi)	0.66	1.27	2.2	2.43
U_∞	(ft/s)	4593.4	4614.6	4618.3	4626.1
M_∞	-	9.68	9.81	9.93	9.96
Re_∞	(10^6/ft)	0.53	1.04	1.82	2.03
Re_2	(10^6/ft)	0.49	0.93	1.61	1.78
ρ_2/ρ_∞	-	5.96	5.97	5.97	5.98
P_{t2}	(psi)	1.22	2.36	4.07	4.51

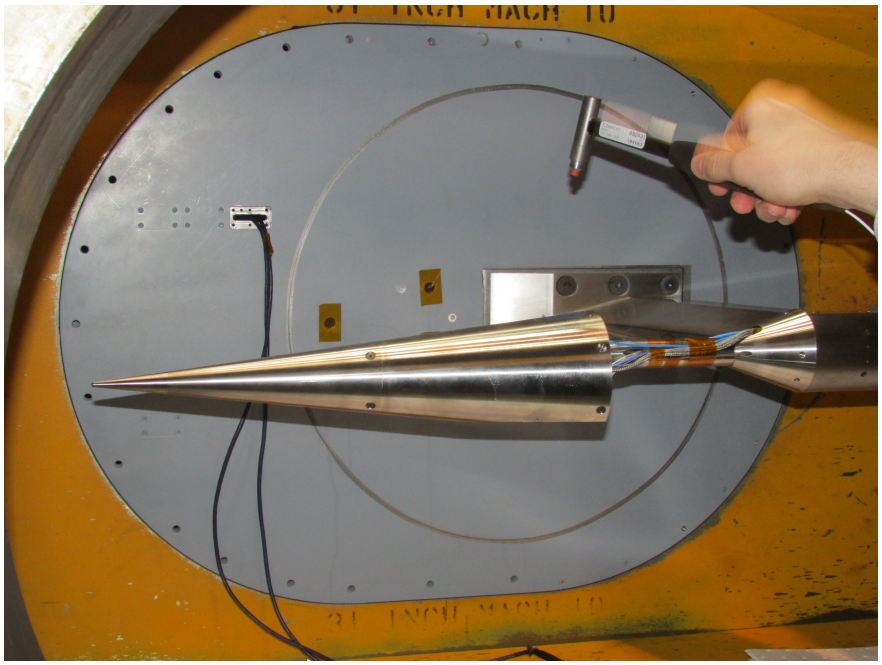


Fig. 2 Test article mounted in the NASA 31-Inch Mach 10 Wind Tunnel [Source: NASA].

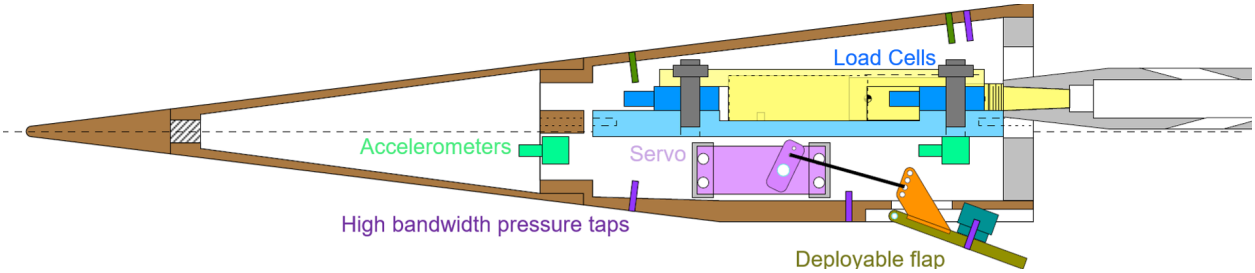


Fig. 3 Sliced view of test article.

for future NASA LaRC endeavors as well. A two dimensional cross section of the cone-slice geometry is shown in Figure 3.

Upon review of this cross section, the inner workings of the test article become more evident. The sting (right) is mounted to the conventional foil strain gauge balance (yellow). This balance is inserted into a balance bore hole within the top balance plate (yellow). Sandwiched between the top and bottom (light blue) balance plates are the three-component piezoelectric strain gauges (blue). The bottom balance plate is constrained to the aft bulkhead (gray) via pins and screws. It is constrained to the front bulkhead, which is a single piece with the aft cone section (brown). With this setup, any load applied to the cone surface is transferred to the bottom plate, through the piezoelectric load cells, to the top plate, through the foil strain gauge balance, and out through the sting. This ensures only a single load path is possible and the full applied force should be recorded by both the foil and piezoelectric strain gauges. Note that custom beryllium copper studs (dark gray and mounted through blue piezoelectric strain gauges) had to be ordered to fit within the space-limited cavity.

The nose tip is interchangeable for specific aerodynamic objectives. The specific flowfield is unimportant for these studies, and therefore, a change in nose tip is not required. The servo (purple) is connected to an arm (orange) on the flap (olive) to rapidly open and close the flap. The flap is nested within the flat slice and contains a high frequency pressure gauge for further information on the load applied during deployment.

All portions of the cone (i.e., cone body, nose tip, bulkheads, flap, and calibration plates) were manufactured from titanium (TI-6AL-4V). This was chosen as it is light weight, provides adequate strength at the maximum predicted temperature, and as a single material to mitigate risk of mismatched thermal expansion. Since dynamic loads are

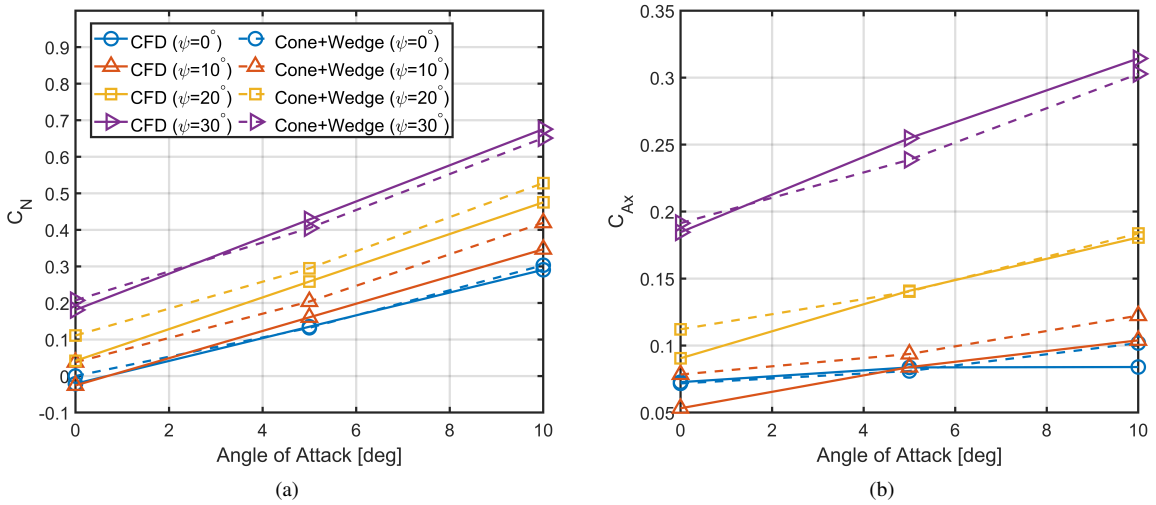


Fig. 4 (a) Normal and (b) axial force coefficient comparison for simplified approximation and CFD analysis.

purposely excited in this study, ensuring reasonable G-loading is critical. Reducing the overall weight helps in this endeavor. The sting is fabricated from steel and houses the cabling and cooling water line for the foil strain gauge balance. Other cabling is placed around the outside of the sting due to the high number of measurements on this test article.

There are a multitude of sensors in this test article, which are depicted in the cross section. First, the conventional foil strain gauge roll balance (yellow) is mounted directly off the sting. This provides highly accurate, calibrated measurement of the quasistatic forces and moments applied with respect to the model center. As dynamic force measurement is of particular interest, model 260A01 PCB piezoelectric strain sensors [22] (blue) are also mounted within the test article. These provide a much higher measurement bandwidth than the typical foil strain gauges. As the SWAT requires acceleration measurement and the other methods benefit from this additional measurement [21], model 356A32 PCB accelerometers [23] (light green) are also mounted within the test article. Two near the rear of the test article, directly below the rear two piezoelectric strain sensors and one mounted on the front bulkhead. High frequency Kulite® pressure sensors, model XCS-093-15A [24] (purple) are mounted in the surface of the cone. One is mounted on the nonflap portion of the slice, one on the cone surface just before the slice and one on the opposite side of the flap. A fourth Kulite® is mounted directly in the flap itself. This particular sensor is a modified 5-wire XCS-093-15A sensor that provides a temperature measurement of the sensor itself. This additional measurement allows for correction of the temperature-dependent frequency response found in these sensors. Finally, temperature measurements are made within the cavity is included to ensure the cavity temperatures remain within the sensor and servo limits. One thermocouple is placed on each balance plate to determine if significant thermal stress is applied across the piezoelectric strain sensors.

C. Expected Loading

Estimating the expected loading is important for the stress analysis of the design as well as the servo selection. Therefore, this subsection is dedicated to estimating the quasisteady forces of the cone-slice model. Begin with the simple estimation of the normal and axial force on a typical 7° half-angle cone. To compute these forces, the normal and axial force coefficients were extracted from a Naval Surface Warfare Center 1975 technical report [25]. This report includes normal and axial force coefficients for a variety of cone angles with half sphere nose tips. Additionally, Mach 10 data are available for 1, 3, 5, and 10 degrees angles of attack.

Next, one can add the flap forcing contribution using tables in NACA 1135 [26] and expected tunnel conditions. The axial and normal force coefficients for a reference area of 14.1863 square inches (circular base area) using this approximation is shown in Figure 4 via the dashed lines. Additionally, NASA personnel performed a laminar CFD analysis on the test article CAD using FUN3D [27] for the various AoA and flap angle combinations of interest. These results are displayed in Figure 4 as well via the solid lines. Note that these results are in family.

For design purposes, the total forces applied to the test article is of interest. This is important both for the safety of

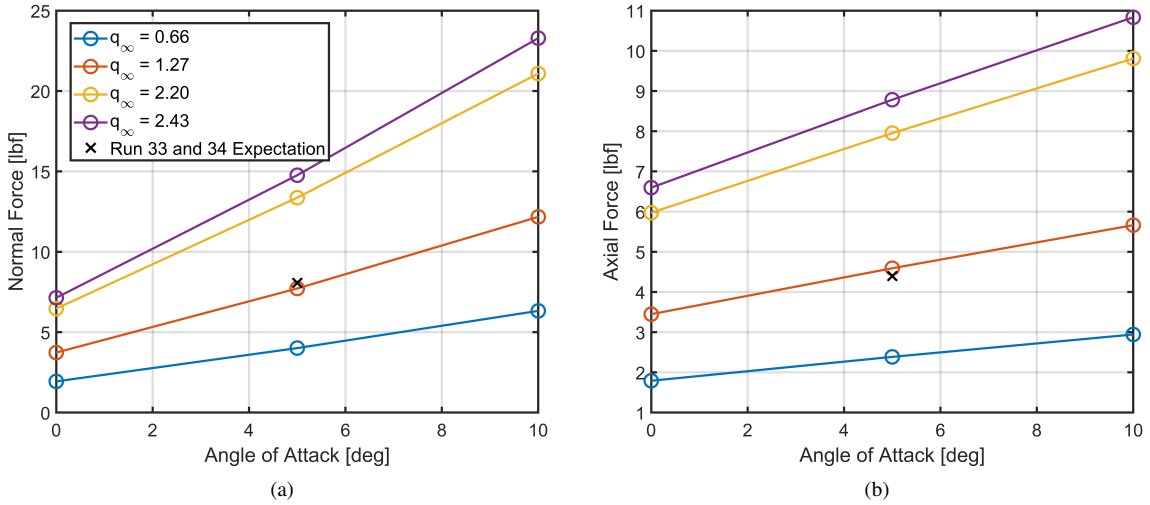


Fig. 5 Full model CFD force estimate using FUN3D in (a) normal and (b) axial directions.

the conventional force balance as well as for the smooth operation of the servo. The worst case loads are for max AoA and flap deflection (purple curve). These coefficients can be converted to forces using

$$F_N = C_N S_{ref} q_\infty \tag{1}$$

$$F_A = C_{Ax} S_{ref} q_\infty \tag{2}$$

with the circular base area as the reference area (4.25" base diameter) and each of the four freestream dynamic pressures given in Table 1.

From a design perspective, the most stressing case is maximum deflection angle, i.e., $\psi = 30^\circ$. This yields the forces in Figure 5 for the four optional tunnel dynamic pressures and AoA. The envelope of the $\psi = 30^\circ$ curve options (purple curves in Figure 4) was used for the coefficients to achieve the most conservative answer. Additionally, the worst case of $\alpha = 10^\circ$ and $\psi = 30^\circ$ force predictions are shown in Table 2. These were below the safety limits of the balance, however, in this study we will focus on slightly less stressing cases to ensure margin. The unknown amplification due to expected load may yield higher forces than this static equilibrium prediction so it is safe to remain well below the balance limits. The two tunnel runs analyzed in this work had tunnel conditions of $q_\infty = 2.2$ psi and test article configurations of $\alpha = 5^\circ$ and $\psi = 20^\circ$. The predicted forces for these conditions are shown with black crosses on Figure 5 for the CFD coefficients as well as for both the CFD and cone-wedge approximation in Table 2.

The authors also predicted the peak forces on the flap and translated the resultant moment to the servo arm. This calculation is omitted from this paper for brevity. However, the levels at the servo are below the stall torque of the selected servo. Additionally, the deployment speed (which is a function of arm torque) is not overly degraded for these worst case loads.

Table 2 Worst case and key tunnel run axial and normal force predictions.

Load	$\alpha = 10^\circ$, $\psi \leq 30^\circ$, $q_\infty = 2.43$ psi	Run 33 and 34: $\alpha = 5^\circ$, $\psi \leq 20^\circ$, $q_\infty = 2.2$ psi	
Method	Worst Case	Full CFD Solution	Cone + Wedge
F_N (lbs)	23.29	8.07	9.20
F_A (lbs)	10.83	4.40	4.38

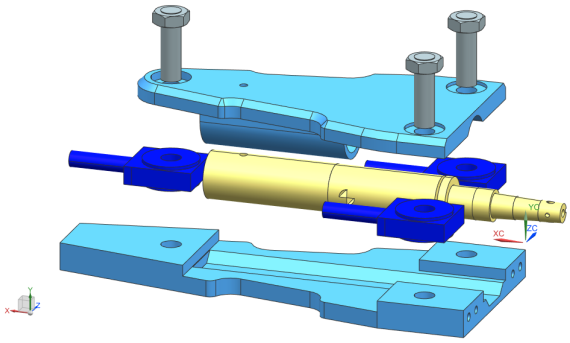


Fig. 6 Exploded isometric view of dynamic force balance.

D. Hybrid Dynamic Force Balance Design

Dynamic force measurement is the primary focus of this research. However, as the static force measurement is not expected to be as accurate as the conventional foil strain gauge roll balance, a hybrid arrangement is developed. The hybrid force balance has highly accurate quasi-static force measurement with the added benefit of high bandwidth dynamic force measurement. This arrangement is inspired by the design used by Draper et al. [3, 28] where the foil strain gauge roll balance, three-component piezoelectric strain gauge sensors, and accelerometers are all used in tandem.

A depiction of the force balance assembly is shown in Figure 6. Due to the conical internal cavity, fitting four load cells, such as the design made by Collopy et al. [29], is not feasible. However, a three sensor arrangement is still capable of measuring all six components of forces and moments, i.e. F_x (Axial), F_y (Side), F_z (Normal), M_x (Roll), M_y (Pitch), and M_z (Yaw).

In the top light blue plate, henceforth referred to as the top balance plate, holds the conventional foil strain gauge roll balance that is affixed to the sting. The bottom light blue plate in Figure 6, henceforth referred to as the bottom balance plate, is constrained to the forward and aft bulkhead. Sandwiched between the two balance plates are three model 260A01 PCB three-component piezoelectric strain sensors. These sensors measure strain in each of the three directions and due to their piezoelectric operation, have a much higher bandwidth than typical strain balances. Typical strain balances have flexures to ensure uniaxial strain that unfortunately limit stiffness. Beryllium-copper studs hold the balance plates together. This metal is used due to its low stiffness but high strength, which ensures that the majority of the load is transferred to the sensing elements rather than the studs. Note that these sensors were originally purchased for AEDC Tunnel 9 use and are therefore of higher magnitude than what would be ideal for this NASA LaRC application.

Finally, triaxial accelerometers are mounted on the bottom of the bottom balance plate as close to the piezoelectric strain sensors as feasible. Acceleration measurements are required by some methods (SWAT) and can be used by other methods (TDDM and FDIM) to enhance result quality. The SWAT requires accelerometer measurements to remove the inertial contribution and for those sensors to be mounted close to the strain measurements to minimize sensor phase delay. For TDDM and FDIM approaches, deconvolution can be performed with acceleration in addition to or rather than strain as the output, as shown by Draper et al. [19].

The design assures that only a single load path exists between the support structure and the model surface. As designed, any aerodynamic load applied to the test article must travel through all strain sensors before reaching the sting and support structure. This ensures maximum signal-to-noise ratio of the strain sensors, which improves the effectiveness of the dynamic force measurement techniques.

E. Dynamic Calibration

To apply the methods discussed in Section IV, one must apply a dynamic calibration to excite the dynamics of the system and map those input-output responses into a useful model for future force estimation. This subsection provides a brief description of the calibration tests performed and the excitation location diagrams of which are referenced in the following sections.

The first set of calibration tests performed were for the SWAT. This method requires both a static and dynamic calibration. To determine the static calibration matrix, a standard weight hanging method, similar to typical wind tunnel testing setups was used [16]. This approach is presented with greater detail in Reference [19]. The setup is shown in

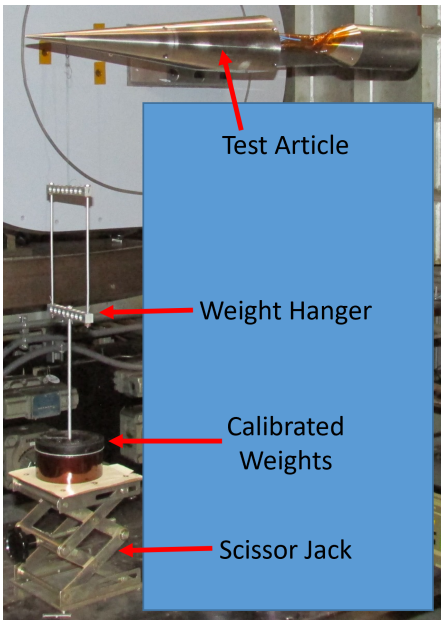


Fig. 7 Example weight hanging calibration setup [Source: NASA].

Figure 7 where the weights are applied along the gravity direction via a screwed connection at various points along the model surface. Unlike typical strain gauges force balances, piezoelectric load cells are capacitive, meaning any applied load will eventually decay back to zero. Therefore, rather than applying the load, steadying the weight, and taking the reading, the weight is smoothly removed via the scissor jack. This imparts error to the static calibration as discussed in Reference [19]. The SWAT dynamic calibration test setup is identical to that shown in Figure 7. However, the line is abruptly severed (via acetylene torch in this case) to impart a dynamic step load and excite a dynamic response of the load cells and accelerometers.

The other set of dynamic calibrations that are required are modal impact hammer inputs. For the TDDM and FDIM approaches, the applied loads must be a point source and precisely known. A modal impact hammer is ideal for this task as these devices have a dynamically calibrated load cell that approximates the true applied load applied at the hammer tip. The target impact locations are shown in Figure 8. A tap was applied at each location a minimum of twelve times to converge the impulse response matrix [21], ensure enough high quality data are available, and to average out errors in location and angle. The softest hammer tip was used to approximate the expected applied load magnitude and pulse width.

IV. Force Reconstruction Methodology Overview

In this section, a brief overview of the SWAT, TDDM, and FDIM is presented. For more in depth information for each method, the reader is encouraged to read Reference [21].

A. SWAT

The first method of interest is the SWAT. This is a two stage method that builds on the commonly used methodology for strain gauge balance calibration. First, as is done for the conventional foil strain gauge roll balance, a static calibration is performed on the piezoelectric strain sensors. This converts the millivolt elastic response of the sensors into elastic force contributions. In the quasisteady scenario, this is approximately the applied force. After this step is performed, a dynamic calibration needs to be applied. In this stage, a dynamic load, which onsets a dynamic response, is required. Typically, a step load is chosen as this more effectively excites the lower frequency modes.

To further understand this, consider the commonly used form of SWAT, to obtain the reconstructed force (F_{rec}), is given by

$$F_{\text{rec}} = S_S C_S + S_A C_A \tag{3}$$

where S_S and S_A are the strain and acceleration response data and C_S and C_A are calibration matrices converting those

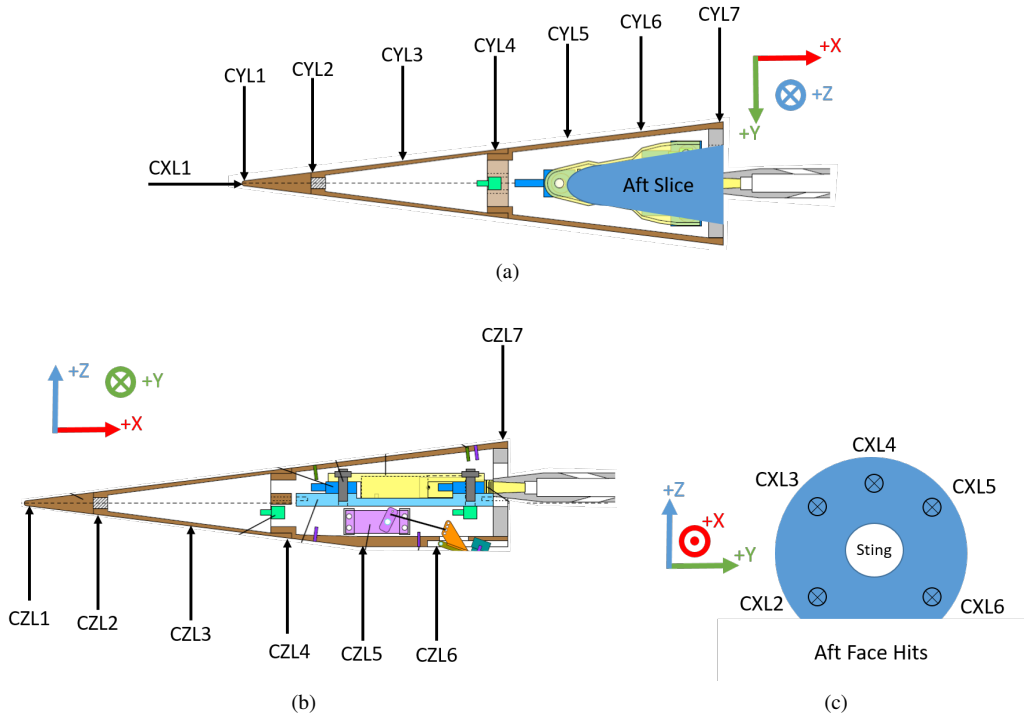


Fig. 8 Hammer tap locations in (a) side, (b) normal, and (c) axial directions for calibration of TDDM and FDIM.

responses into forces. In this form, one may recognize the similarity to a single degree of freedom (SDOF) spring-mass system. Typical force measurement assumes proportionality between strain and applied force, and therefore, the strain response, S_S, can be scaled by a static calibration matrix, C_S, similar to the stiffness of an SDOF system. However, when the system is not at steady state, the equation of motion contains an inertial term. Note that the damping contribution is assumed small and neglected from this explanation but can be accounted for by using measured or derived strain rate or velocity data.

In previous research, Draper et al. [3] reformulated this commonly used method to account for the fact that each mode of vibration may be excited to a different degree. Therefore, applying only one scaling matrix to the entirety of the acceleration signal may be insufficient. Instead, we choose to scale each frequency of the signals separately, given by

$$F_{\text{rec}} = S_S C_S + \Sigma_{l=1}^{L} S_{A,l} C_{A,l} \tag{4}$$

where each mode of the inertial response, $C_{A,l}$, obtained via filtering or curve fitting of the acceleration signal, is scaled separately and combined with the scaled strain response. Note that one must decide on a max number of modes (L) to consider. In Reference [3], it was found that higher frequency modes of the acceleration response are phase shifted to a small degree with respect to the strain response. This means that no amount of scaling can ever remove the unwanted inertial effects. Therefore, this sensor response delay problem presents an inherent upper frequency limit of this method.

An important note about this method is that the recovered forces and moments are computed with respect to the moment center. Therefore, if a particular force magnitude at a particular location is of interest, this method will only reconstruct the total forces and moments, similar to the static measurement methodology. This may be undesirable for point force problems such as lateral air jets. The following two methods are point force reconstruction methods.

B. TDDM

This method is somewhat of a divergence from the force reconstruction methodologies typically used in wind tunnel testing. In TDDMs, time domain proportionality is no longer assumed. Rather, for linear time invariant (LTI) systems, there exists an impulse response function (IRF) relating an input force location and output measurement location (e.g., individual strain or acceleration channel). This is advantageous as only a single measurement type is required. However, the formulation is significantly more complex and computationally expensive.

In TDDMs, the mechanism for generating this relationship is the convolution of the applied force with the IRF and defined as

$$y(t) = \int_0^t h(t-\tau)u(\tau)\mathrm{d}\tau = h * u(t) \tag{5}$$

where the output, $y(t)$, at time t is the convolution between the input, $u(t)$, and the IRF, $h(t)$. This equation can represent any LTI system. For our application, we may utilize this for the assumed LTI relationship between applied force and measured strain. The strengths of this method are that it only requires one measurement (acceleration data not needed) and phase shifts are inherently accounted for in the IRF. The chief weakness of this family of methods is that the entire force history from $t = 0$ is needed, and therefore, can be a rather large computation. Therefore, TDDMs are ideal for short duration, impulsive tests such as the pulsed forcing discussed in this research.

To solve Eq. (5), we need the IRF and a way to deconvolve the IRF from the measured strain response. Therefore, the problem under investigation is actually the inverse of Eq. (5) where the input is the unknown. A typical solution of this problem assumes a discrete form of Eq. (5) and generates a "convolution matrix" from a known IRF. A similar approach will be used in this research, however, proposed by Draper et al. [18], where a higher order discretization is assumed, transforming the continuous representation of the convolution integral into

$$y(t_k) = \sum_{i=0}^{N}\left[\sum_{j=0}^{M}\begin{bmatrix} h_{k-i\cdot R_2-j} & h_{k-i\cdot R_2-j-1}\end{bmatrix}\int_{s_h=0}^{s_h=1}\mathbf{N}_h\hat{\mathbf{N}}_u\mathrm{d}s_h\right]\mathbf{u}_{i+1}\Delta t_s. \tag{6}$$

This distribution can be linear, quadratic, or cubic and is captured in the $\mathbf{N}$ matrices. Next, this discrete equation can be assembled into matrix form as

$$\mathbf{y} = \hat{\mathbf{B}}\mathbf{u}\Delta t_s, \tag{7}$$

and solved by inverting the $\hat{\mathbf{B}}$ matrix and multiplying it by the measured strain or acceleration channel, $\mathbf{y}$. Note, a constraint parameter of $R_2 > 1$ is selected to ensure this matrix has many more rows than columns. Therefore, a least squares pseudoinverse can be employed to solve this inversion. Note that the IRF must be known prior to this solution. However, the convolution formulation is cumulative. Therefore, the roles of u and h can be switched in all previous equations and one may solve for the IRF given a known applied dynamic load. Typically, a hammer pulse is chosen for this load as impulse hammers are commonly used and can excite a wide bandwidth of dynamics.

C. FDIM

This final method of interest is the FDIM. This is a frequency domain couple to the TDDM. As such, it is based on the same physics as in that method. However, the solution procedure is performed in the frequency rather than time domain. The primary advantage of this approach is that much longer time histories may be used. The computational complexity grows considerably for TDDMs. However, the frequency domain formulation in this method allows for a much simpler solution.

Again one may begin with the convolution given by Eq. (5). However, rather than discretizing this equation, a Fourier transform is performed on both sides of the equation. Performing this transformation yields

$$Y(\omega) = H(\omega)U(\omega) \tag{8}$$

where the complex convolution of two time domain signals becomes a more simplified multiplication of two frequency domain signals (denoted with capital variables). Each frequency contribution of the unknown applied load can be solved by dividing the corresponding frequency contribution of the measurement by that of the IRF, i.e.,

$$U(\omega) = \frac{Y(\omega)}{H(\omega)}. \tag{9}$$

Finally, an inverse Fourier transform yields the applied input force in the time domain.

Similarly to the TDDM, the frequency response function (FRF – the Fourier transform of the IRF) is required to solve for an input force. As in the TDDM, this operation is commutative. Therefore, we may solve for the FRF given a known applied dynamic input such as a hammer pulse. To obtain the FRF, simply swap the roles of U and H in Eq. (9). To get the time domain IRF (if desired), perform an inverse Fourier transform of the result.

One additional modification considered here is that the IRF/FRF holds for any input and output measured at the same location [21]. Therefore, many tests may be stacked together to simultaneously solve for the FRF of interest, i.e.,

$$\begin{pmatrix} Y_1 \\ Y_2 \\ \vdots \\ Y_p \end{pmatrix}_{\omega} = \begin{pmatrix} U_1 \\ U_2 \\ \vdots \\ U_p \end{pmatrix}_{\omega} H(\omega) \tag{10}$$

where the equation becomes overconstrained. As desired, we may solve this equation using a least squares pseudoinverse. The least squares inversion technique [30] is chosen to perform the pseudoinverse for this work.

V. Real World Considerations

Prior to presenting the results of each method, it is useful to discuss some of the real world considerations that affect force reconstruction for the wind tunnel application. Some of these considerations include cavity temperature gradients, distributed loading, aeroelastic forcing, and signal-to-noise ratio (SNR). These real world effects affect the measurement hardware and reconstruction accuracy which can ultimately introduce errors and uncertainty into the results.

A. Cavity Temperatures

Typical experiments in this tunnel utilize a water cooled strain balance and surface mounted pressure and temperature sensors. However, in this experiment, additional sensors are present that have no temperature shielding. The piezoelectric strain and acceleration sensors have an operational temperature range of -65 to 250°F, so the first challenge is to ensure the max operating temperature will not be exceeded (which could lead to sensor damage). However, there are other problems related to thermal load that affect force reconstruction. First, these sensors have temperature dependent responses affecting their sensitivity to applied load at different temperatures. This implies that a calibration performed at room temperature can become invalidated if the sensors heat up (or equivalently cool down) and yield a different response to an applied load. Although we may correct for this via cavity temperature measurement, it is preferred to keep the temperatures near room temperature. Another concern is thermal strain. These strain sensors are intended to measure mechanical strain between two surfaces (and force via calibration), however, they have no mechanism for differentiating mechanical and thermal strain. Therefore, a difference in temperature between the two plates (or even between the sensor and a plate) could cause a false response which will not be a mechanical applied load of interest. Finally, the servos also have a limited temperature range. Most manufacturers claim a maximum operating temperature of approximately 140°F. Therefore, the servo will likely fail prior to any sensors if the cavity temperatures become too high.

To monitor temperatures for sensor safety and thermal strain, a thermocouple was placed on each of the upper and lower balance plates. The time histories over the entire 30 second test for wind tunnel runs 33 and 34 (single triangle flap pulse and pulse and flap hold for five seconds, respectively) are shown in Figure 9. There is significant scatter in the temperature readings. NASA data acquisition experts and test engineers believe this is most likely electromagnetic interference (EMI) caused by the servo. Although the team made their best effort at shielding the servo from the other cables, some EMI is still expected due to all cables having to run down the same sting. Although there is scatter in the data, the trends are still clear as evidenced by the solid, filtered traces in each figure.

Note that the starting temperature of the upper plate is lower for both tests. This is expected since the strain gauge roll balance is mounted within the upper plate and is water cooled. Therefore, one may expect higher conductive cooling of the upper plate relative to the lower plate. For both test cases, the overall temperature rise of the balance plates is small ($< 2^{\circ}$F). Therefore we expect the response sensitivity due to termperature rise to be negligible. Additionally, the temperatures remain well below the failure temperatures of the servo and sensors. Finally, the temperature difference between the upper and lower plates is also minimal ($< 1^{\circ}$F) for both tests. Therefore, one may expect minimal thermal strain across the piezoelectric load cells.

B. Distributed Loading

To this point, we have discussed point force loading. In wind tunnels, loading is via the flow, and therefore, distributed in nature. Ideally, if one knows the load is distributed, one could attempt to use the point force contributions to reconstruct the pressure loading. Based on preliminary numerical experiments as discussed in Reference [21], it is

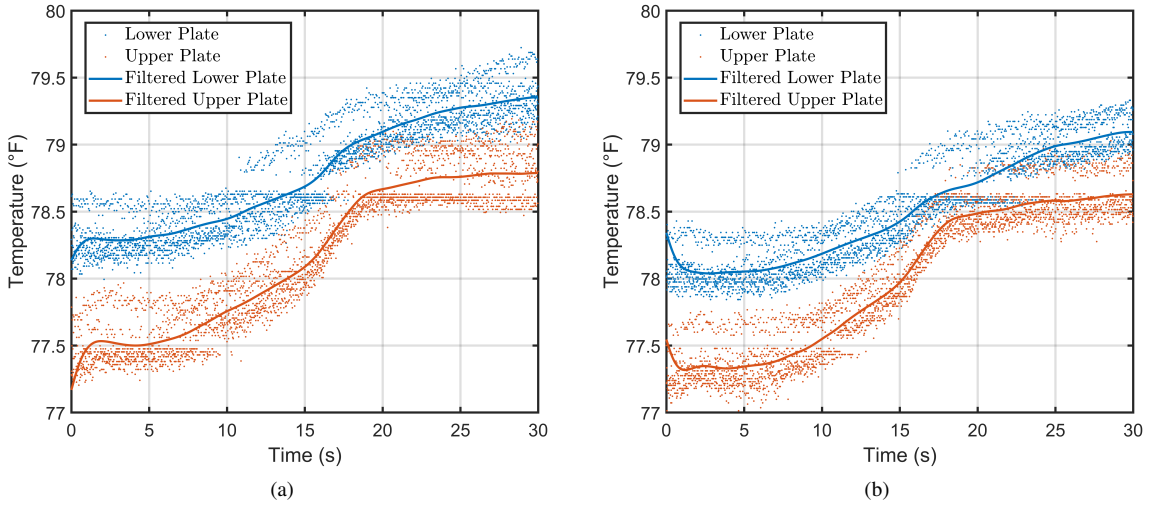


Fig. 9 Upper and lower plate temperatures during (a) pulse test run 33 and (b) ramp-hold test run 34.

possible to reconstruct a dynamic pressure field given a sufficiently dense grid of reconstructed point forces. However, this has yet to be validated on an experimental system. For this analysis, we will assume the pressure load supplies a near equivalent concentrated force. This is typically done in static analyses of distributed loading. Although this is not exact for the dynamic case, it can provide a decent approximation. Future work may explore pressure reconstruction over the flap where it is expected that the distributed load will be quite nonuniform.

In the case of the pressure force being perfectly uniform (though still time variant), it is valid to assume an equivalent point force. This is demonstrated in Reference [21] where a dynamic pressure load (triangle pulse) was applied to the flap of a simulated representation of the test article in Abaqus. The test article and distributed load on the flap (red arrows) are shown in Figure 10.

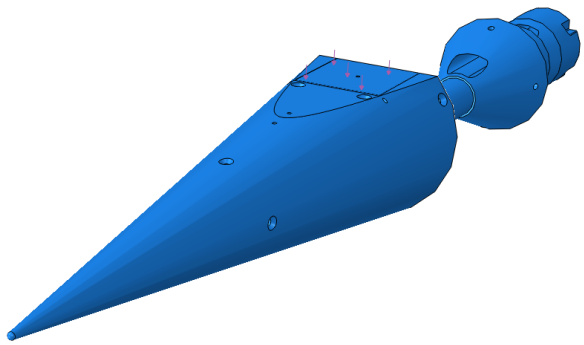


Fig. 10 Abaqus FEM with distributed pressure loading on flap denoted by red arrows.

C. Aeroelastic Loading

A Large contributor to uncertainty is aeroelastic loading. During a wind-off or no-flow test, the dynamics (e.g., impulse response function, stiffness, damping) of an LTI system are predictable and repeatable. However, when the same system is subjected to an aerodynamic load at a high Mach number, the dynamics of the system change due to a coupling between elastic deformation and aerodynamics. Of particular concern is the deformation-dependent aerodynamic load due to bending flexibility of the flap as it gets deployed. If the aeroelastic effects are significant relative to the magnitudes of the applied load, they may dwarf the target measurement.

D. Signal and Tunnel Noise

Arguably the largest contributor of error and uncertainty in force reconstruction is noise. In a perfect testing scenario, one should try to maximize the usable sensor range relative to the expected applied load. This will ensure that the root mean squared noise is far from the signal of interest and the signal quality will be excellent. However, there are other forms of noise beyond this ambient electrical noise that can cause signal obstruction. One such example is tunnel noise [31, 32], which causes localized vibrations on the test article. These low level vibrations are often acceptable for a quasi-static test where the vibrations can be averaged. However, it can be detrimental when the oscillations are on the order of the applied load (see discussion in Subsection V.C).

Measurement noise was very evident on this test. For example, consider Figure 11. In this test, the flap was pulsed inside the wind tunnel under both wind off (left) and wind on (right) conditions. In the wind off scenario, dynamics of the system (primarily the first few modes between 10 and 100 Hz) are excited and quickly damp out. However, in the wind on scenario, many modes are evident throughout the entire time history. Although the pulse is still evident in both the time history and magnitude scalogram, the ambient tunnel noise is of a much higher magnitude than desired.

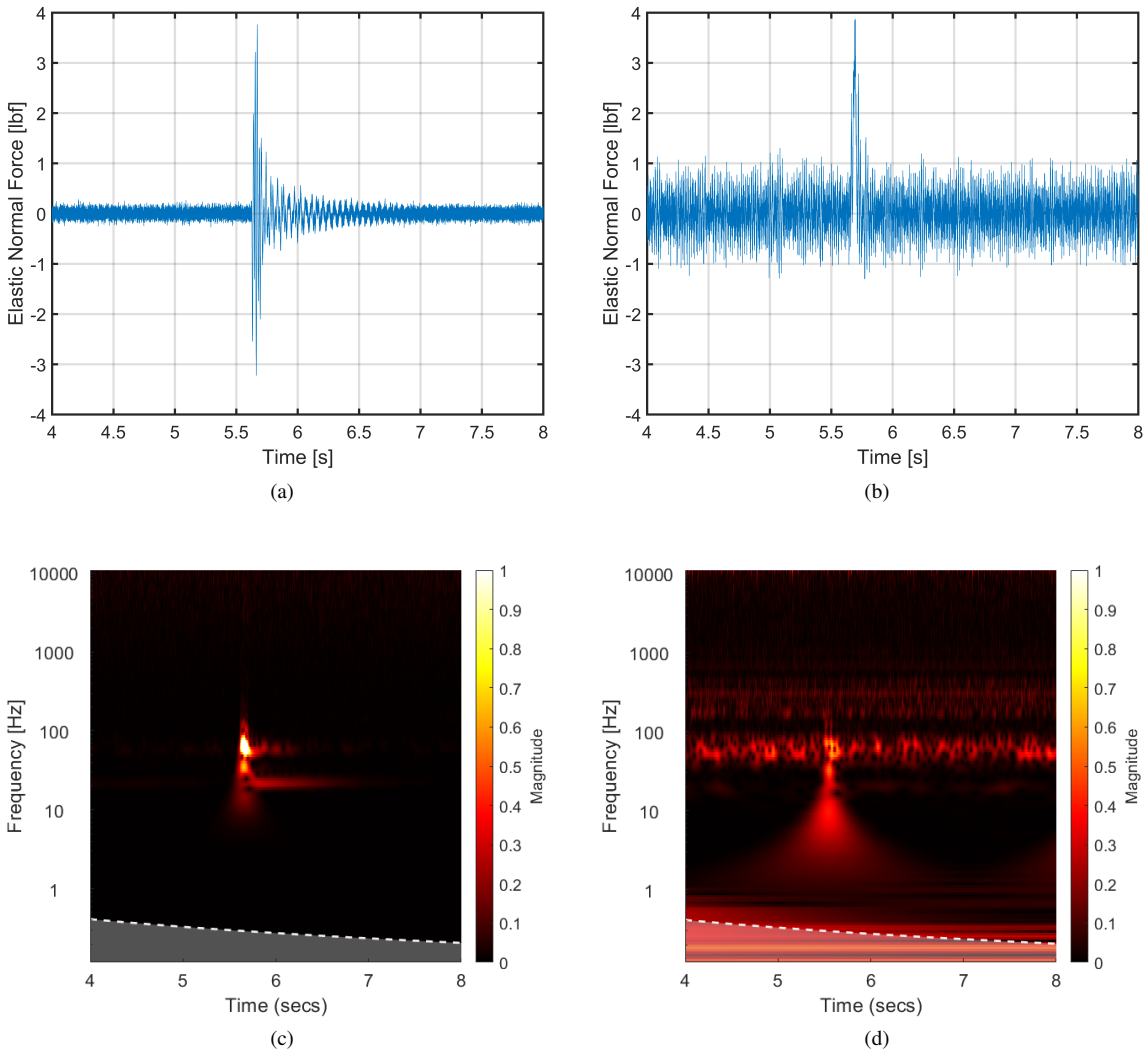


Fig. 11 Strain gauge measurement (normal force channel) time histories (top row) and scalograms (bottom row) for a wind off (left column) and wind on (right column) pulse test.

VI. Dynamic Force Reconstruction Results

This section details the preliminary results of each method. Speculation on error from expected results as well as recommendations for future work are discussed for each method.

A. SWAT Results

To demonstrate the SWAT approach, the ramp (i.e., pulse deflection and hold) from Run 34 was used. Since SWAT is a simple matrix multiplication technique, one may easily apply it to an entire time history. In Figure 12, the entire time history, i.e., test article injection ($T = 2$s), flap deployment ($T = 7$s), flap retraction ($T = 12$s), and test article removal ($T = 17$s), is shown. For this analysis, the elastic force contribution was computed using standard, first-order NASA methodology rather than statically calibrated piezoelectric strain gauge force rings. This is because (1) the hanging weight static and dynamic calibrations were unable to apply side and pure axial forces as well as yawing moments and (2) the signal-to-noise ratio on the piezoelectric strain sensors was very low.

Three frequency ranges over which to determine separate acceleration calibration matrices were selected based on the the observed frequency response during drop test dynamics calibration. Those ranges were $f < 30$ Hz, $30 \leq f < 50$ Hz, and $50 \leq f < 80$ Hz. Therefore, all frequency content above 80 Hz is low pass filtered from both the reconstructed and (for fair comparison) the elastic force and moment data. After reviewing the elastic force and moment data (blue curves) obtained using standard, first-order NASA wind tunnel calibration methods, it is clear that the oscillations induced by the ramp applied load (starting at $T = 7$s) do not greatly exceed that of the general tunnel noise prior to and after the ramp deployment. Therefore, few residual oscillations are observed beyond the magnitude of the ambient noise and the SWAT result (red) seems similar to the elastic force.

Interestingly, over the more severe applied forces of test article injection and retraction, one can observe reduction of the residual oscillations in the reconstructed traces. A zoomed view of Figure 12 over the test article retraction phase is plotted in Figure 13. Note the considerable reduction of the pitch and yaw applied loads in particular. This demonstrates the SWAT approach is still useful, however, the applied loads may need to be higher relative to the ambient tunnel noise for the effectiveness to be realized.

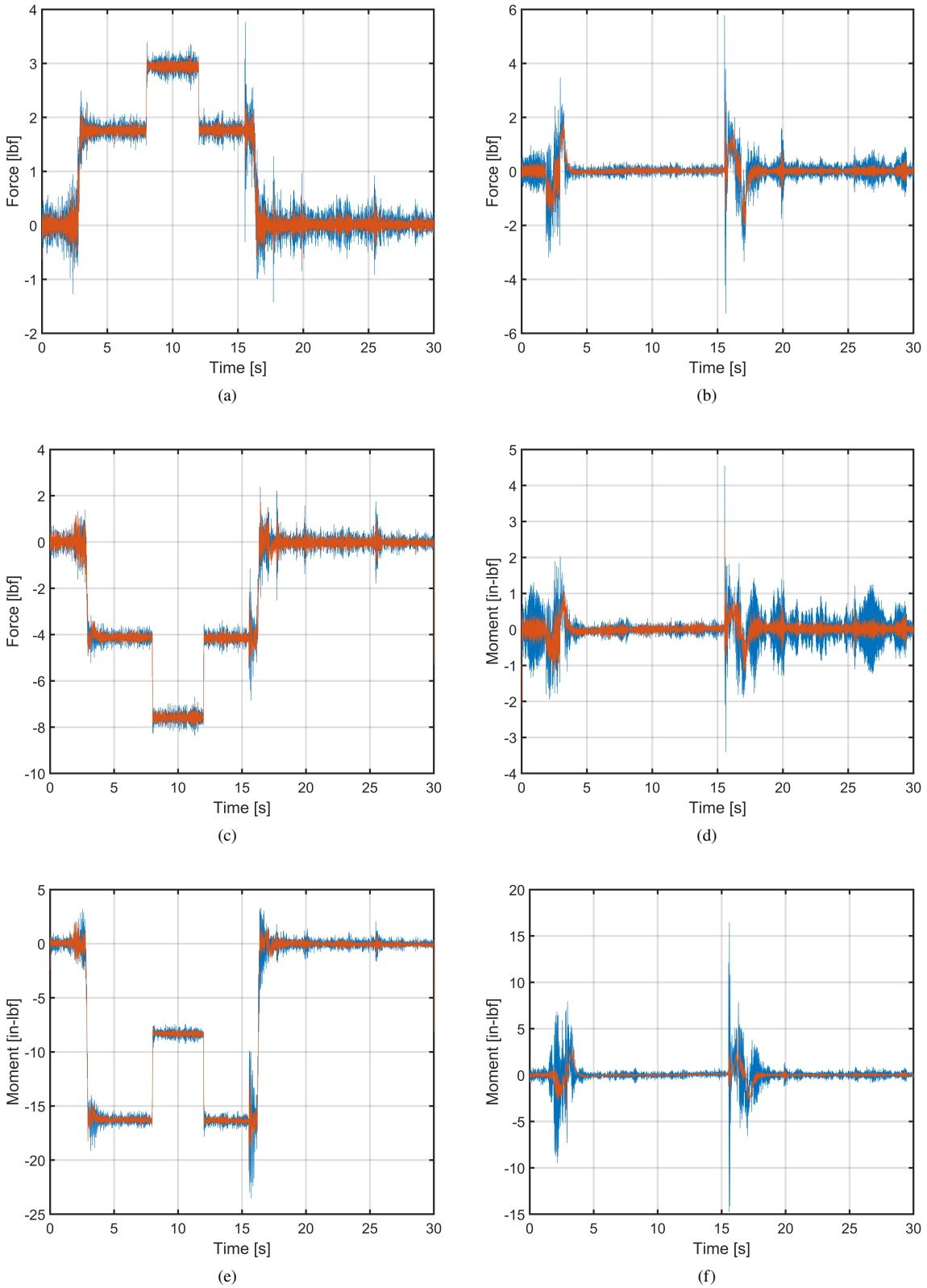


Fig. 12 SWAT force reconstruction results in (a) axial, (b) side, and (c) normal directions and moment results in (d) roll, (e) pitch, and (f) yaw.

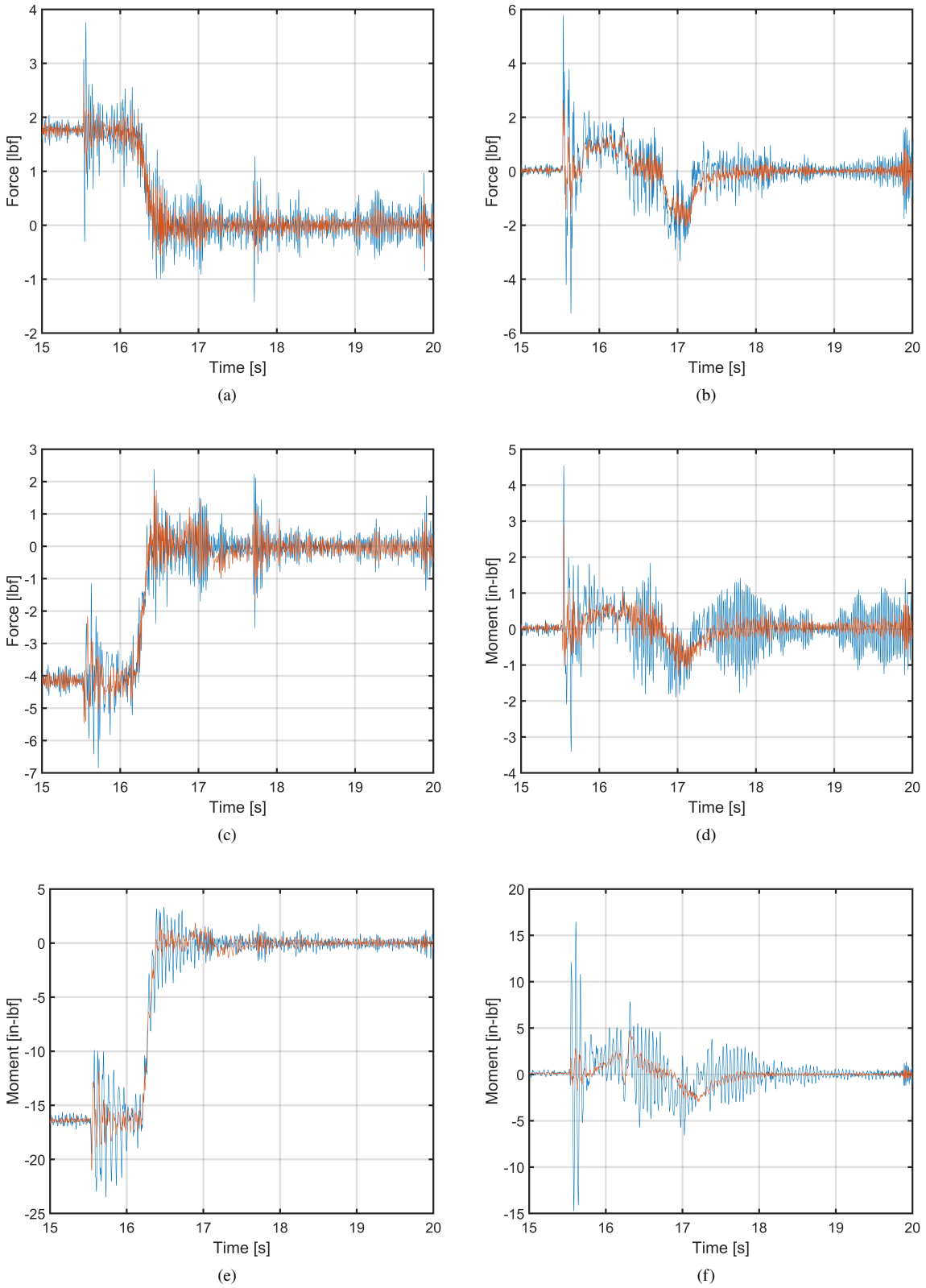


Fig. 13 Zoomed view of SWAT force reconstruction results from 15 to 20 seconds in (a) axial, (b) side, and (c) normal directions and moment results in (d) roll, (e) pitch, and (f) yaw.

B. TDDM Results

To demonstrate the TDDM method, the first pulse of Run 33 was used. This run was a fast triangle pulse of the flap into the windward side of a 5° angle-of-attack flow with nominal conditions of Condition 3 from Table 1. A longer time history of the normal force channel of the strain gauge roll balance can be seen in Figure 11b. To approximate the flap position, the aft point, hinge, and flap edge locations were tracked every two milliseconds over the pulse duration. The resultant flap angle and angle-of-attack estimates are shown in Figure 14a. Note that this is not a perfect triangle pulse, but rather more of a smoothed out trapezoid. The measured elastic force using the conventional six component roll strain gauge balance is shown in blue in Figure 14b-d. Note that significant oscillations are observed both due in part to tunnel noise and the desired, applied dynamic load.

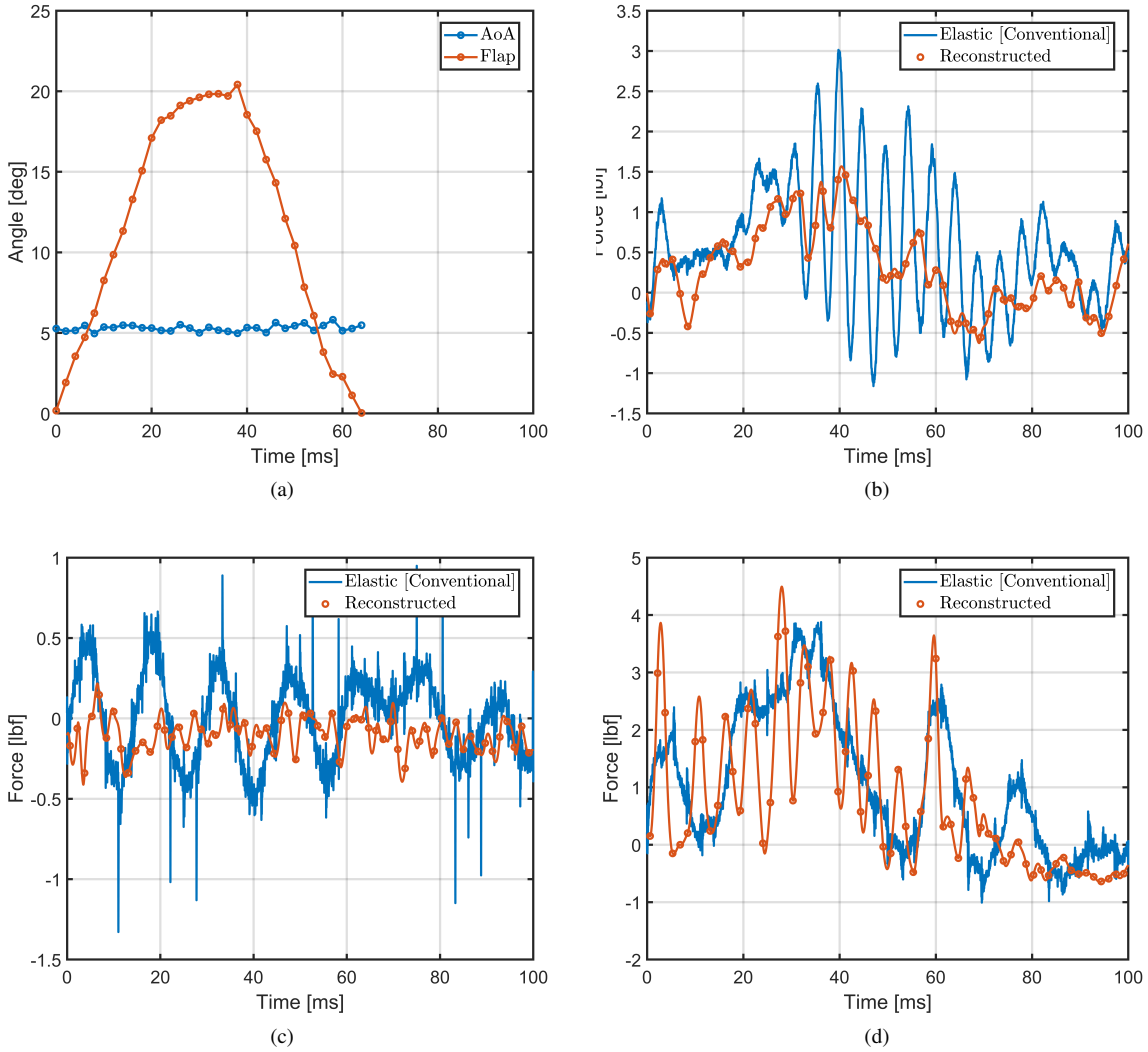


Fig. 14 (a) Angle measurements and TDDM pulse reconstruction results in (b) axial, (c) side, and (d) normal directions.

The reconstructed pulses at calibration locations CXL1, CYL7, and CZL6 (see Figure 8) are shown in red in Figure 14b-d, respectively. The constraint parameter and order for this analysis are $R_1 = R_2 = 20$ and order$= 3$. The axial force reconstruction appears to be rather successful where the substantial elastic oscillations measured by the axial channel of the conventional strain gauge are removed and a more triangular pulse is recovered. There are still subsequent oscillations in the reconstruction that can be attributed to either error or aeroelastic forcing contributions. A similar observation may be noted for the side force reconstruction (Figure 14c) where the overall magnitude of the oscillations

are reduced substantially from the elastic force, but residual oscillations remain. The normal force reconstruction is the least clear. Large amplitude oscillations remain and large spikes near the beginning and end of the pulse are evident. An approximation of the angle of attack at the flap is shown via the blue curve in Figure 14a. Although there is uncertainty in the manual measurement of this from high speed video, the state does appear to be oscillating – indicating a state dependent normal and axial force is likely present (i.e., aeroelastic forcing).

To better understand the normal force trace, the data from a wind off pulsed flap were investigated. In Figure 15, the reconstructed normal force at location CZL6 is compared to the normal force strain channel (elastic force). Note that at

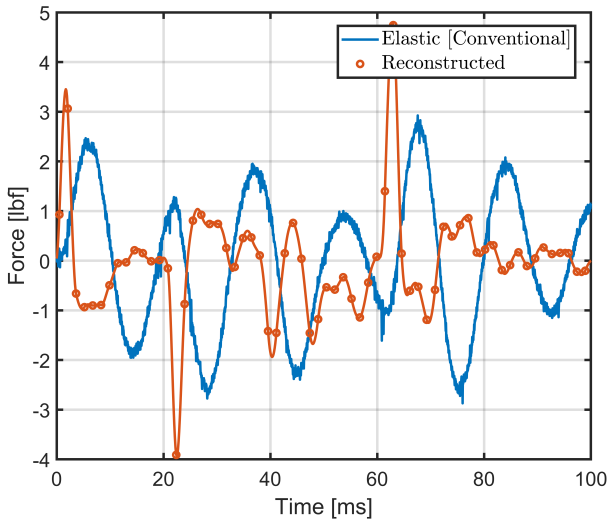


Fig. 15 Wind off normal force reconstruction.

the time of flap deployment (0 ms) and return (60 ms), there are large positive normal force spikes. Additionally, there is a clear negative normal force spike when the flap reaches full deployment (20 ms). Characteristically similar spikes are observed in Figure 14d. These forces are real, servo-induced loads, which cause a dynamic response of the test article. Therefore, the load applied to the centroid is a combination of (1) the aerodynamic load applied by the flap deployment and quasi-static angle of attack, (2) the aeroelastic loading of the oscillating test article, and (3) the internal loading of servo actuation. Therefore, the reconstructed normal force may be difficult to interpret with the combined loading of all three components. Future studies should be performed to separate these forcing contributions.

C. FDIM Results

The same test case (Run 33) used in Section VI.B is used for FDIM demonstration due to its similarity with TDDM methods. This is a single triangle pulse of similar magnitude and duration to the applied pulses during dynamic calibration. The results using FDIM are shown in Figure 16. As expected, the results are very similar to those in

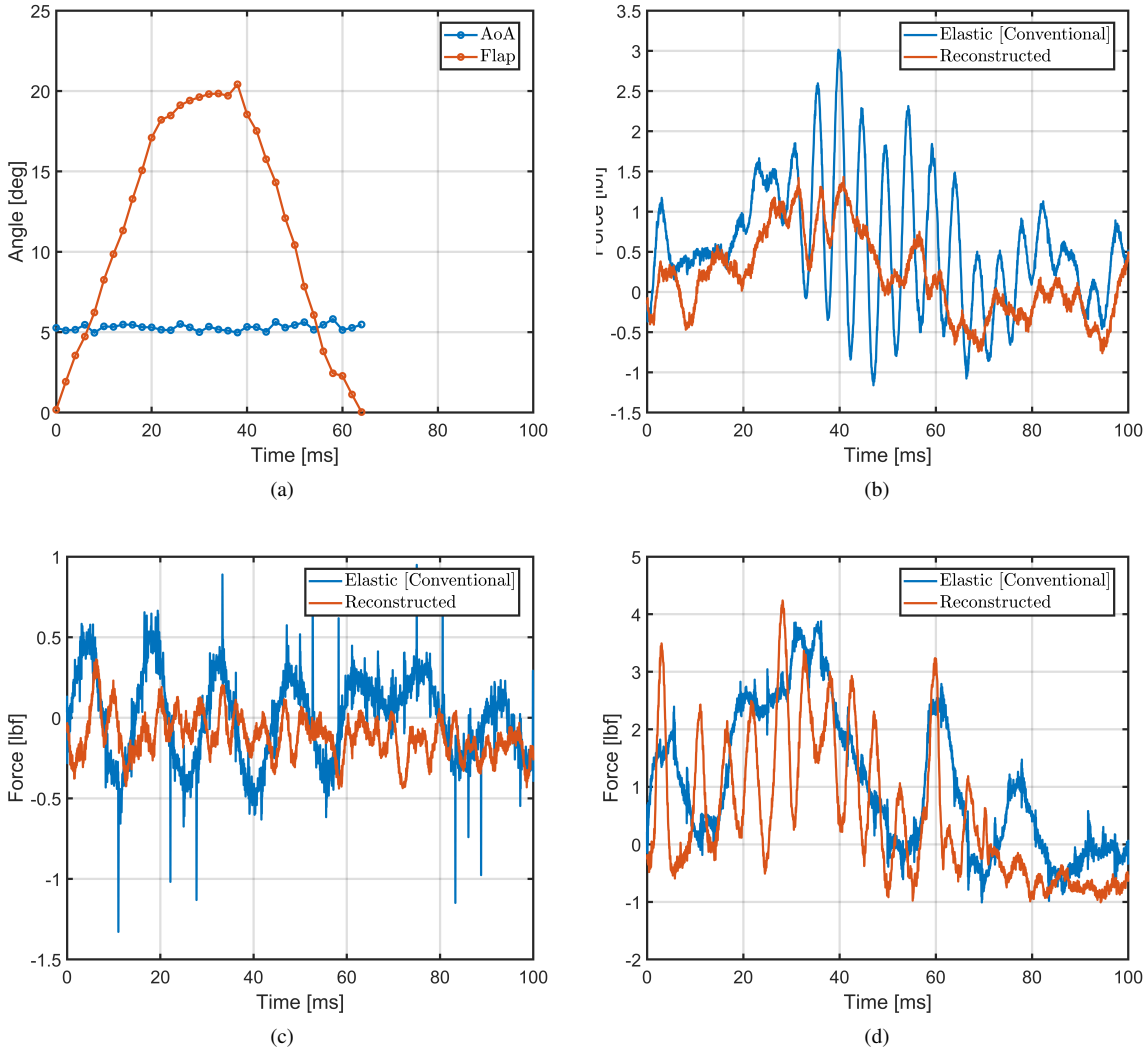


Fig. 16 (a) Angle measurements and FDIM pulse reconstruction results in (b) axial, (c) side, and (d) normal directions.

Figure 14. The same calibration set and test data (Run 33) were used for this reconstruction so it is not surprising that the results agree with TDDM estimates. The conclusions remain the same as those stated in Section VI.B. Specifically in the normal direction, once again a combination of the applied triangle load, the pulses of servo activation, and aeroelastic forcing contributions are combined to complicate the resultant force.

VII. Conclusion

In this work, three force reconstruction methodologies, SWAT, TDDM, and FDIM, were demonstrated on an induced dynamic load at the NASA Langley Research Center 31-Inch Mach 10 wind tunnel. A flap was embedded within the surface of an aft slice of a seven degree half-angle titanium cone test article. This flap could be rapidly deployed via an internally mounted servo to apply flap deflection angles of interest. In this work, the design of the test was described in addition to initial results for each method.

The initial results presented in this work for each method are promising but further analysis is needed. Although the residual tunnel oscillations are reduced for each method, there are complicating factors such as internal servo forcing, tunnel noise, and aeroelastic forcing which make it difficult to determine the true applied load, and therefore, whether each method was accurate. Future work should explore separating out these various contributions and attempt a distributed load estimate using all inputs of the point force methods.

Acknowledgments

The first author thanks the Arnold Engineering Development Complex (AEDC) Wind Tunnel No. 9 for funding the initial design of this test article and providing dynamic measurement sensors; and thanks the internal APL external publication and presentation (EPP) program for providing the funding to complete this work.

References

[1] Marineau, E. C., "Force Measurements in Hypervelocity Flows with an Acceleration Compensated Piezoelectric Balance," *Journal of Spacecraft and Rockets*, Vol. 48, No. 4, 2011, pp. 697–700. https://doi.org/10.2514/1.A32047, URL http://arc.aiaa.org/doi/10.2514/1.A32047.

[2] Marineau, E., MacLean, M., Mundy, E., and Holden, M., "Force Measurements in Hypervelocity Flows with an Acceleration Compensated Strain Gage Balance," *Journal of Spacecraft and Rockets*, Vol. 49, No. 3, 2012, pp. 474–482. https://doi.org/10.2514/1.A32041, URL http://arc.aiaa.org/doi/10.2514/1.A32041.

[3] Draper, J. W., Lee, S., and Marineau, E. C., "Development and Implementation of a Hybrid Dynamic Force Measurement System at AEDC Tunnel 9," American Institute of Aeronautics and Astronautics, 2017. https://doi.org/10.2514/6.2017-1593, URL http://arc.aiaa.org/doi/10.2514/6.2017-1593.

[4] Mee, D. J., Daniel, W. J. T., and Simmons, J. M., "Three-component force balance for flows of millisecond duration," *AIAA Journal*, Vol. 34, No. 3, 1996, pp. 590–595. https://doi.org/10.2514/3.13108, URL http://arc.aiaa.org/doi/10.2514/3.13108.

[5] Mee, D. J., "Dynamic calibration of force balances for impulse hypersonic facilities," *Shock Waves*, Vol. 12, No. 6, 2003, pp. 443–455. https://doi.org/10.1007/s00193-003-0181-6, URL http://link.springer.com/10.1007/s00193-003-0181-6.

[6] Ngo, C., Powell, J., and Ross, J. C., "Inverse Force Determination on a Small Scale Launch Vehicle Model using a Dynamic Balance," *55th AIAA Aerospace Sciences Meeting*, American Institute of Aeronautics and Astronautics, Grapevine, Texas, 2017. https://doi.org/10.2514/6.2017-1405, URL http://arc.aiaa.org/doi/10.2514/6.2017-1405.

[7] Grauer, J. A., and Boucher, M. J., "Frequency-Domain Deconvolution for Flight Dynamics Applications," *2018 Atmospheric Flight Mechanics Conference*, American Institute of Aeronautics and Astronautics, Atlanta, Georgia, 2018. https://doi.org/10.2514/6.2018-3157, URL https://arc.aiaa.org/doi/10.2514/6.2018-3157.

[8] Sanderson, S. R., and Simmons, J. M., "Drag balance for hypervelocity impulse facilities," *AIAA Journal*, Vol. 29, No. 12, 1991, pp. 2185–2191. https://doi.org/10.2514/3.10858, URL http://arc.aiaa.org/doi/10.2514/3.10858.

[9] Doherty, L. J., Smart, M. K., and Mee, D., "Measurement of Three-Components of Force on an Airframe Integrated Scramjet at Mach 10," American Institute of Aeronautics and Astronautics, 2015. https://doi.org/10.2514/6.2015-3523, URL http://arc.aiaa.org/doi/10.2514/6.2015-3523.

[10] Laurence, S., Martinez Schramm, J., Karl, S., and Hannemann, K., "An Experimental Investigation of Steady and Unsteady Combustion Phenomena in the HyShot II Combustor," American Institute of Aeronautics and Astronautics, 2011. https://doi.org/10.2514/6.2011-2310, URL http://arc.aiaa.org/doi/10.2514/6.2011-2310.

[11] Laurence, S., Ozawa, H., Lieber, D., Martinez Schramm, J., and Hannemann, K., "Investigation of Unsteady/Quasi-Steady Scramjet Behavior using High-Speed Visualization Techniques," American Institute of Aeronautics and Astronautics, 2012. https://doi.org/10.2514/6.2012-5913, URL http://arc.aiaa.org/doi/10.2514/6.2012-5913.

[12] Resch, L., Zentz, L., and Allwine, J., "Hypersonic shroud separation testing and modelling capabilities at the Naval Surface Warfare Center hypervelocity wind tunnel 9," American Institute of Aeronautics and Astronautics, 1994. https://doi.org/10.2514/6.1994-2495, URL http://arc.aiaa.org/doi/10.2514/6.1994-2495.

[13] Dagan, Y., and Arad, E., "Analysis of Shroud Release Applied for High-Velocity Missiles," *Journal of Spacecraft and Rockets*, Vol. 51, No. 1, 2014, pp. 57–65. https://doi.org/10.2514/1.A32489, URL http://arc.aiaa.org/doi/10.2514/1.A32489.

[14] Lazur, A., Sawyer, J., Sullivan, B., and Hudson, L., "Hypersonic vehicle control surface development," *9th International Space Planes and Hypersonic Systems and Technologies Conference*, American Institute of Aeronautics and Astronautics, Norfolk,VA,U.S.A., 1999. https://doi.org/10.2514/6.1999-4864, URL http://arc.aiaa.org/doi/10.2514/6.1999-4864.

[15] Falkiewicz, N., Cesnik, C., Bolender, M., and Doman, D., "Thermoelastic Formulation of a Hypersonic Vehicle Control Surface for Control-Oriented Simulation," *AIAA Guidance, Navigation, and Control Conference*, American Institute of Aeronautics and Astronautics, Chicago, Illinois, 2009. https://doi.org/10.2514/6.2009-6284, URL http://arc.aiaa.org/doi/10.2514/6.2009-6284.

[16] Internal Balance Technology Working Group (ed.), *Recommended Practice: Calibration and Use of Internal Strain-Gage Balances with Application to Wind Tunnel Testing (AIAA R-091-2003)*, American Institute of Aeronautics and Astronautics, Inc., Washington, DC, 2003. https://doi.org/10.2514/4.476464, URL http://arc.aiaa.org/doi/book/10.2514/4.476464.

[17] Berger, K. T., Hollingsworth, K. E., Wright, S. A., and Rufer, S. J., "NASA Langley Aerothermodynamics Laboratory: Hypersonic Testing Capabilities," *53rd AIAA Aerospace Sciences Meeting*, American Institute of Aeronautics and Astronautics, Kissimmee, Florida, 2015. https://doi.org/10.2514/6.2015-1337, URL http://arc.aiaa.org/doi/10.2514/6.2015-1337.

[18] Draper III, J., and Lee, S., "Smooth construction of impulse response functions and applied loads using a time domain deconvolution method," *Journal of Sound and Vibration*, Vol. 443, 2019, pp. 430–443. https://doi.org/10.1016/j.jsv.2018.11.050, URL https://linkinghub.elsevier.com/retrieve/pii/S0022460X18308149.

[19] Draper, J. W., and Lee, S., "Development of Hypersonic Wind Tunnel Force Measurement using Deconvolution of Acceleration Data," *AIAA Scitech 2019 Forum*, American Institute of Aeronautics and Astronautics, San Diego, California, 2019. https://doi.org/10.2514/6.2019-0940, URL https://arc.aiaa.org/doi/10.2514/6.2019-0940.

[20] Sanchez, J., and Benaroya, H., "Review of force reconstruction techniques," *Journal of Sound and Vibration*, Vol. 333, No. 14, 2014, pp. 2999–3018. https://doi.org/10.1016/j.jsv.2014.02.025, URL https://linkinghub.elsevier.com/retrieve/pii/S0022460X14001527.

[21] Draper III, John Willis, "Dynamic Force Measurement in Hypersonic Wind Tunnels," Dissertation, University of Maryland, College Park, 2019. URL https://drum.lib.umd.edu/handle/1903/25119.

[22] "PCB Model 260A01," , ????. URL https://www.pcb.com/Products.aspx?m=260A01.

[23] "PCB Model 356A32," , ????. URL https://www.pcb.com/Products.aspx?m=356A32.

[24] "XCS-093.pdf," , ????. URL https://www.kulite.com/assets/media/2018/01/XCS-093.pdf.

[25] Morrison, A. M., *Handbook of inviscid sphere-cone flow fields and pressure distributions*, Naval Surface Weapons Center, Naval Surface Weapons Center, White Oak Laboratory, White Oak, Silver Spring, Marlyand, 1975. URL http://books.google.com/books?id=LyMIQ8j863MC, oCLC: 1103316605.

[26] Field, M., "EQUATIONS, TABLES, AND CHARTS FOR COMPRESSIBLE FLOW," NACA 1135 - Annex 6B, 1991.

[27] "FUN3D Manual," , ????. URL https://fun3d.larc.nasa.gov/.

[28] Draper, J., Lee, S., and Marineau, E., "Numerical construction of impulse response functions and input signal reconstruction," *Journal of Sound and Vibration*, Vol. 432, 2018, pp. 259–271. https://doi.org/10.1016/j.jsv.2018.06.041, URL https://linkinghub.elsevier.com/retrieve/pii/S0022460X18304036.

[29] Collopy, A., Lee, S., and Marineau, E. C., "Development of Dynamic Force Measurement Capabilities at AEDC Tunnel 9," American Institute of Aeronautics and Astronautics, 2014. https://doi.org/10.2514/6.2014-0983, URL http://arc.aiaa.org/doi/10.2514/6.2014-0983.

[30] Peters, G., and Wilkinson, J., "The Least Squres Problem and Pseudo-Inverses," *The Computer Journal*, Vol. 13, No. 3, 1970.

[31] Laganelli, A., and Howe, J., "Prediction of Pressure Fluctuations Associated with Maneuvering Re-entry Weapons," Tech. Rep. AFFDL-TR-77-59, Jul. 1977.

[32] Casper, K., Beresh, S., Henfling, J., Spillers, R., Pruett, B., and Schneider, S., "Hypersonic Wind-Tunnel Measurements of Boundary-Layer Pressure Fluctuations," *39th AIAA Fluid Dynamics Conference*, American Institute of Aeronautics and Astronautics, San Antonio, Texas, 2009. https://doi.org/10.2514/6.2009-4054, URL https://arc.aiaa.org/doi/10.2514/6.2009-4054.